

CONSTRAINING THE HIGH DENSITY NUCLEAR SYMMETRY ENERGY WITH PIONS

By

Justin Estee

A DISSERTATION

Submitted  
to Michigan State University  
in partial fulfillment of the requirements  
for the degree of

Physics – Doctor of Philosophy

2019

**ABSTRACT**

CONSTRAINING THE HIGH DENSITY NUCLEAR SYMMETRY ENERGY WITH PIONS

By

Justin Estee

Copyright by  
JUSTIN ESTEE  
2019

## **ACKNOWLEDGEMENTS**

Your acknowledgements here.

## TABLE OF CONTENTS

LIST OF TABLES . . . . .	vi
LIST OF FIGURES . . . . .	vii
CHAPTER 1 EXPERIMENT . . . . .	1
1.1 Operational Principles of Time Projection Chambers . . . . .	1
1.2 S $\pi$ RIT TPC Overview . . . . .	2
1.2.1 Enclosure . . . . .	4
1.2.2 Field Cage . . . . .	4
1.2.3 Voltage Step Down . . . . .	9
1.2.4 Wire Planes . . . . .	9
1.2.5 Pad Plane . . . . .	14
1.2.6 Electronics . . . . .	14
1.3 Energy loss in material . . . . .	15
1.3.1 Gas Properties . . . . .	16
1.4 Pad Response Function . . . . .	18
1.4.1 Experimental Pad Response Function . . . . .	20
1.4.2 Considerations when constructing a TPC . . . . .	21
1.5 Ancillary Detectors . . . . .	23
1.5.1 Kyoto Multiplicity Trigger . . . . .	23
1.5.2 Krakow KATANA Veto and Multiplicity Array . . . . .	24
1.5.3 Active Veto Array . . . . .	25
1.6 Radio Isotope Beam Factory (RIBF) Facility . . . . .	25
1.7 Experimental Setup . . . . .	26
1.8 Data Acquisition (DAQ) . . . . .	27
1.9 Trigger Condition . . . . .	28
1.10 Collision Data Taken . . . . .	31
APPENDIX . . . . .	32
BIBLIOGRAPHY . . . . .	35

## LIST OF TABLES

Table 1.1	An overview of the properties of the S $\pi$ RIT TPC . . . . .	4
Table 1.2	Wire plane properties . . . . .	9
Table 1.3	Summary of range of GET electronics settings. . . . .	15
Table 1.4	. . . . .	18
Table 1.5	Primary and secondary beam properties produced in the S $\pi$ RIT TPC experimental campaigns. . . . .	27
Table .1	List of runs for the analysis. . . . .	33

## LIST OF FIGURES

Figure 1.1 Operation principle of the TPC . . . . .	2
Figure 1.2 Overview of the S $\pi$ RIT TPC . . . . .	3
Figure 1.3 FC overview . . . . .	5
Figure 1.4 FC overview 2 . . . . .	6
Figure 1.5 Schematic of the TPC system . . . . .	7
Figure 1.6 Schematic of the electric connections relevant to the Field Cage system. The strip thickness is exaggerated in the figure to show the detail . . . . .	8
Figure 1.8 On and off configurations of the gating grid. . . . .	11
Figure 1.10 Number of electrons produced in a single avalanche on an anode wire. Two different voltages were simulated using Garfield++ at 1470 V and 1214 V. The expected Polya distribution fit is also given in yellow. . . . .	13
Figure 1.11 Drift velocity of electrons in P10 gas. . . . .	17
Figure 1.12 A cartoon illustration of the charge distribution resulting from an electron avalanche on one wire and the projections of the distribution onto the two axis $\rho(x)$ onto the x-axis and $\rho(z)$ onto the z-axis. The orientation of the wire planes is flipped upside down to display the perspective better. . . . .	19
Figure 1.13 Experimental pad response function of many events for a crossing angle of $85^\circ < \theta \leq 90^\circ$ . . . . .	21
Figure 1.14 PRF response from $\pi^-$ data. . . . .	22
Figure 1.15 Parameters $N_0$ and $\sigma$ as a function of the crossing angle $\theta$ with the 4 <sup>th</sup> order polynomial fits. . . . .	23
Figure 1.16 Exploded views of Kyoto and KATANA arrays. . . . .	24
Figure 1.17 Overview of the RIBF, BigRIPS, and SAMURAI beamline. . . . .	26
Figure 1.18 Drawing of the experimental setup with the TPC inside of the SAMURAI magnet at 0° configuration. . . . .	28
Figure 1.19 KATANA trigger box logic. . . . .	29
Figure 1.20 Master trigger logic. . . . .	29

## CHAPTER 1

### EXPERIMENT

#### 1.1 Operational Principles of Time Projection Chambers

Time projection chambers are a class of detectors which reconstruct charged particles in all 3-dimensions. Here we will outline the physical principles involved in the TPC measurement and discuss the particular details of the TPC used in this thesis. Inside of at TPC the detector gas is housed in a field cage, which also sets up a constant electric field. As charged particles pass through the gas, electron-ion pairs from neutral gas molecules by passing tracks; the electrons are accelerated opposite to the electric field and the ions move in the opposite direction. Since the mean free path of the electrons inside the gas is very small, they quickly collide with other gas molecules, slowing down the electron, which is then accelerated again repeating the cycle. This microscopic behavior manifests into a constant drift velocity when averaged over several gas collisions. These electrons drift up towards a set of wire planes eventually reaching a set of high voltage anode wires where they accelerate under the high electric field, liberating more electron-ion pairs from the gas creating an avalanche. The avalanche electrons finally terminate either on the anode wire or the grounded pad readout plane, while the ions from the avalanche move slowly away from the anode wires; creating a large signal which is distributed over the pad-plane where the charge and time information of the signal is measured by the electronics.

Two of the 3 coordinates are determined from the charge distribution on the pad plane. The third dimension comes from projecting the electrons back in time, utilizing the known constant drift velocity  $v_d$ ; the distance the electron has traveled ,  $d$ , – along the electric field direction– is calculated as  $d = v_d \cdot t$ , where  $t$  is the time it took for the electrons to reach the electronics. The radius of curvature is related to the magnetic rigidity, and therefore the momentum of each track. The energy loss deposited ( $\langle dE/dx \rangle$ ) is measured by the segmented charge sensitive pads on the pad-plane, which are connected to the readout electronics. Particle identification is achieved

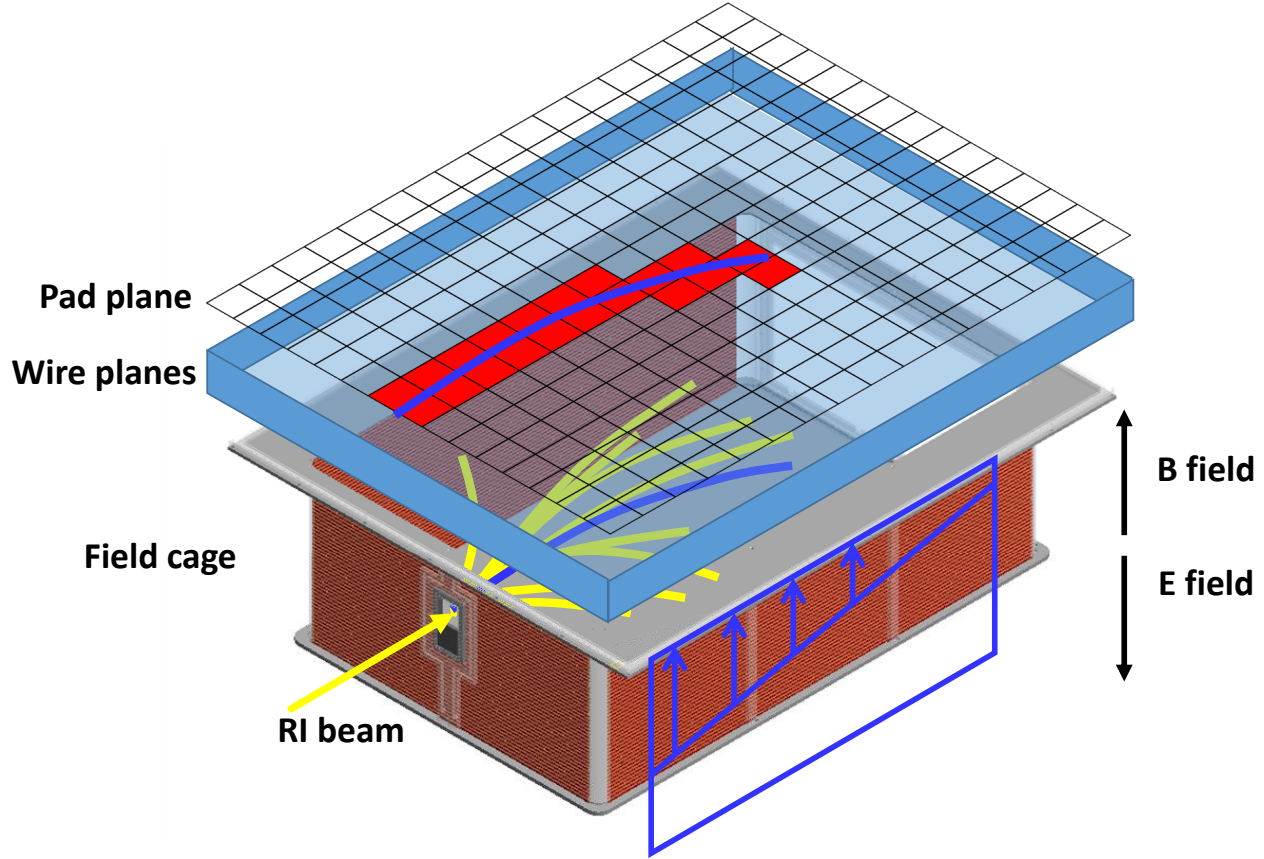


Figure 1.1: Operation principle of the TPC

through since unique particles exist on unique rigidity and  $\langle dE/dx \rangle$  lines, which will be discussed in latter sections. In this chapter we will discuss in more detail the process described above in the context of the specific TPC used in this thesis.

## 1.2 S $\pi$ RIT TPC Overview

The Samurai Pion-Reconstruction and Ion Tracker Time Projection Chamber (S $\pi$ RIT TPC) is a multi-wire proportional counter developed to measure pions and other light charge particles resulting from radioactive heavy ion collisions in fixed target experiments. The TPC is built on an aluminum angle iron skeleton with thin aluminum sheet walls all around, in order to minimize neutron scattering and to allow for light charged particles to reach auxilliary detectors on the sides

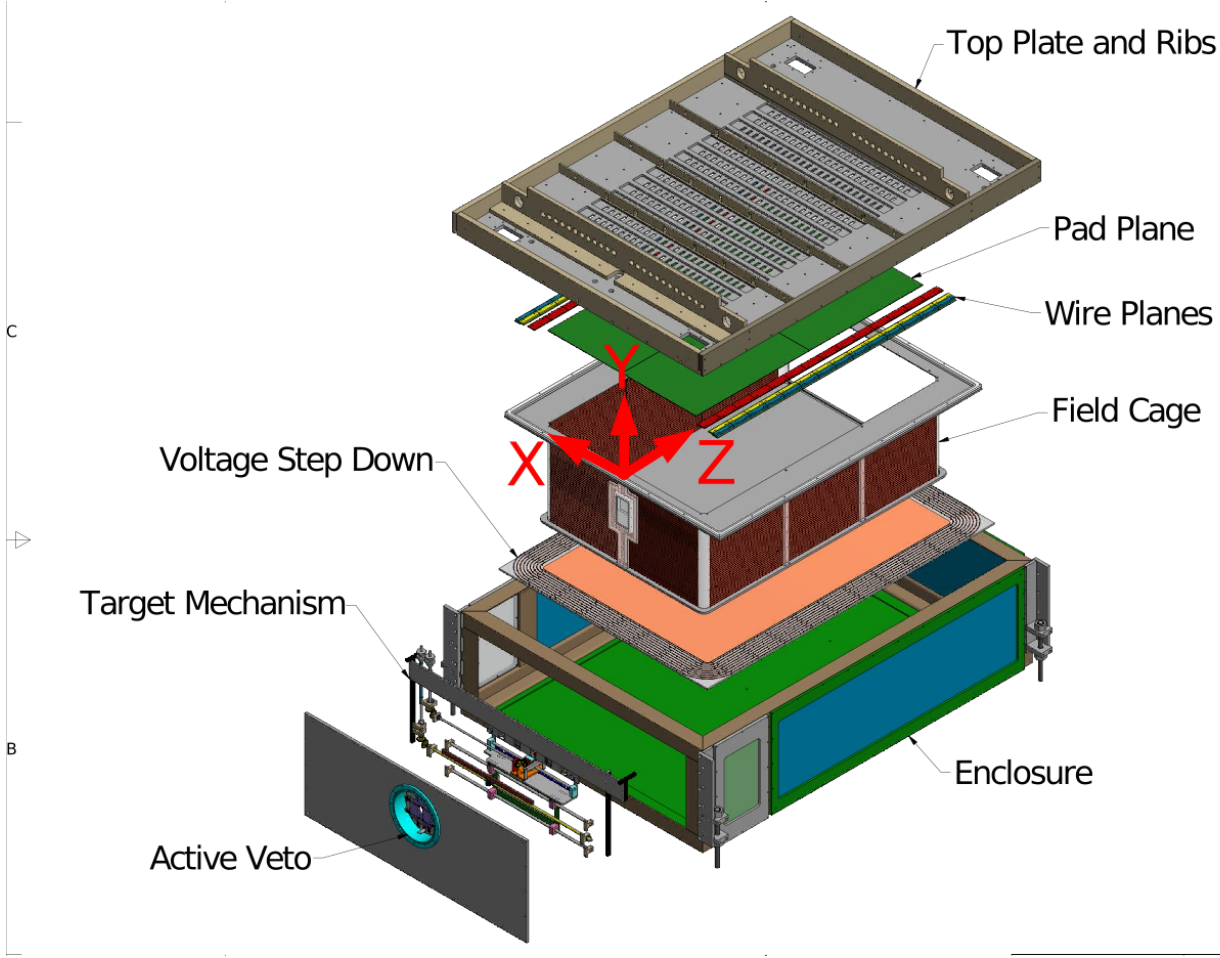


Figure 1.2: Overview of the S $\pi$ RIT TPC

and downstream of the TPC. The S $\pi$ RIT TPC was developed to fit inside the SAMURAI dipole magnet used at the Rare Isotope Beam Factory (RIBF) at RIKEN in Wako-shi, Japan [1]; the dipole gap limited the vertical space of the TPC to around 75 cm. More detail and specifications of the SAMURAI dipole magnet are given in [2].

A target mechanism allowed for up to 5 fixed targets to be mounted at anytime, with the ability to change targets on the outside of the TPC. The field cage contained the detector gas and set up the constant electric field, which was mounted to a large aluminum top plate, though electrically isolated by a lexan top perimeter ring with o-rings to provide as gas seal. The pad plane and wire plane structures are also mounted to the inside face of the top plate with the electronics being mounted on the outside face of the top plate; several aluminum ribs were also mounted to provide

S $\pi$ RIT TPC Overview	
Pad plane area	1.3 m x .9 m
Pad size	1.2 cm x .8 cm
Number of pads	12096 (112 x 108)
Gas composition	90% Ar + 10% CH <sub>4</sub> (1 atm)
Multiplicity limit	200
dE/dx range	Z=1-3, $\pi$ , p, d, t, He, Li
Drift length	50 cm

Table 1.1: An overview of the properties of the S $\pi$ RIT TPC

extra rigidity to the top plate, keeping it flat to within 150  $\mu$ m, as measured by a laser [3]. Holes on the top plate allowed for the readout of the individual charge sensitive pads on the pad plane, through surface mount pads which were connected through short cables to the electronics. The exploded drawing shown in Fig. 1.2 pictures all of the major internal components of the of the S $\pi$ RIT TPC

### 1.2.1 Enclosure

The skeleton of the enclosure is composed of a rigid aluminum angle-iron frame. All walls are constructed of a aluminum frame with thin sheet metal. All materials were made to be as thin to allow charged particles and neutrons to exit the TPC without scattering too much. This allows for a trigger to be created by placing detectors on the sides and downstream of the TPC. The enclosure itself is made to be gas tight with respects to the outside and the field cage. This is to allow for the possibility to run a different gas inside the enclosure than the field cage. Although, in this set of experiments we ran the same gas in the field cage and enclosure volume.

### 1.2.2 Field Cage

The field cage contains the detector gas and sets up a uniform electric field in which electrons can drift upwards toward the anode wires. It was designed to hang from the top plate and therefore

needed to be of a lightweight construction. The materials needed to be thin to allow for light charged particle and neutrons to pass through without significant scattering for ancillary detectors.

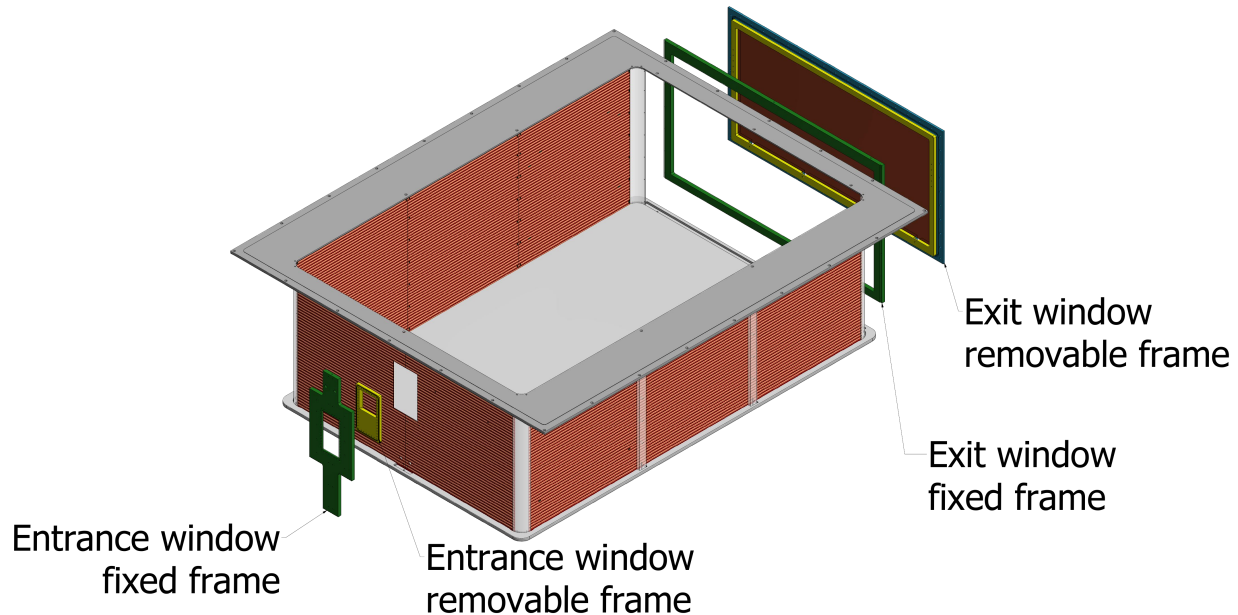


Figure 1.3: FC overview

The field cage was constructed from several panels of printed circuit boards (PCBs). The front of the field cage was made of two PCBs and each side was constructed of three PCBs supported by Lexan pieces. The epoxy in the common PCB substrate FR4 contains bromine which is not suitable for the long term operation of a TPC, as the bromine will eventually cause gain reduction of the wires CITE HERE. The halogen free material used was Cryogenic-G10. The field cage is an isolated volume from the enclosure of the TPC for the option to run explosive gases such hydrogen in the field cage, where the enclosure can be filled with an insulating gas. While the risk of a high voltage spark was minimized using the voltage step down, the risk of sparking when using an explosive gas could be further minimized by isolating the detector volume from the enclosure volume thereby allowing you to run an insulating gas between the field cage while running the explosive gas inside the detector volume only. Instead of a downstream wall, a large

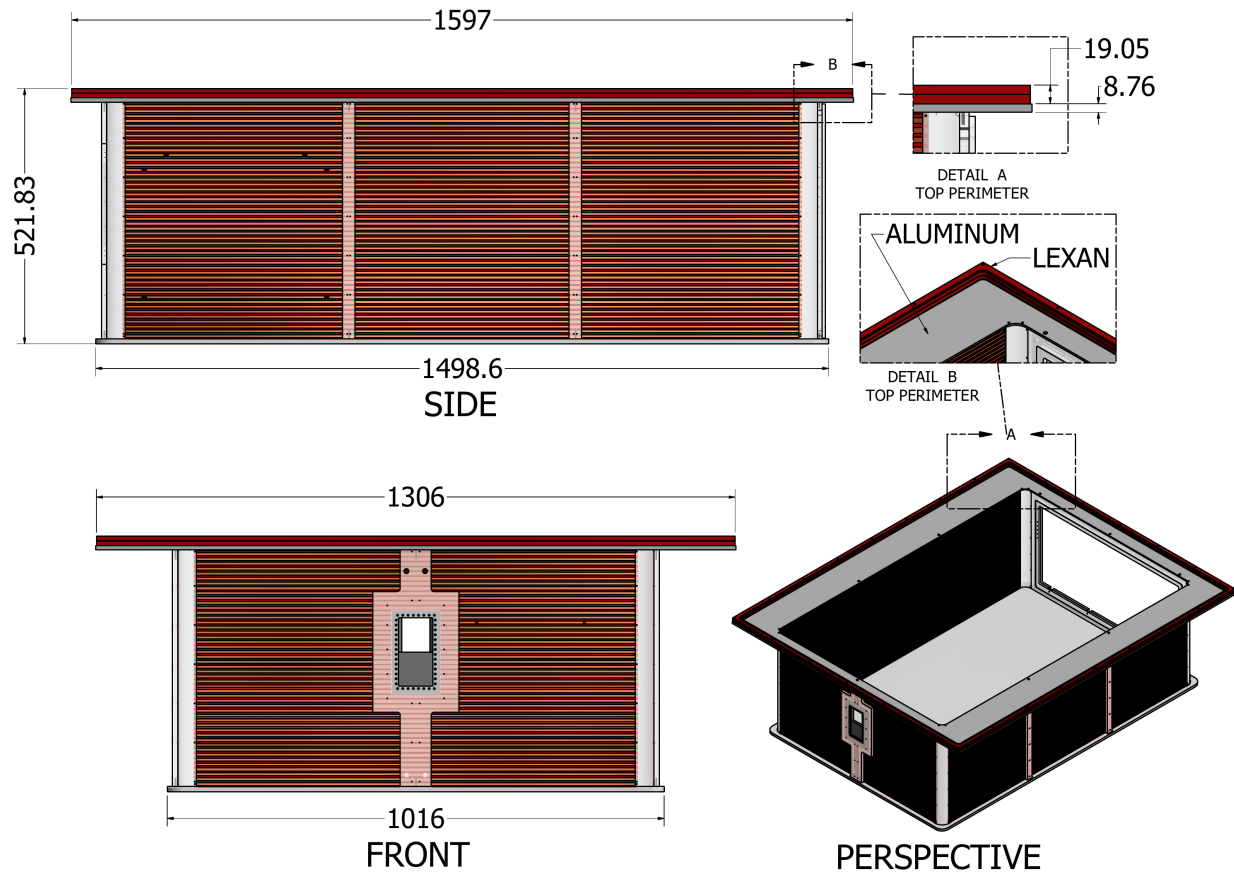


Figure 1.4: FC overview 2

thin exit window was constructed which consisted of a lexan frame bonded to a  $10\text{ }\mu\text{m}$  Kapton window with evaporated aluminum strips. The PCB boards were epoxied into the cathode which was constructed of an aluminum honeycomb laminate where two sheets of aluminum were bonded to a core of aluminum honeycomb structure providing a lightweight yet rigid structure. On the other end the boards were epoxied into an aluminum top perimeter which also served as the last ring in the TPC. Together with the cathode bottom, the field cage proved to be a rigid lightweight structure. A lexan ring containing o-rings was placed in-between the top perimeter piece and the top plate of the TPC. Screws with nylon washers, and collars, were used to mount the top perimeter, and the field cage, to the top plate. The top plate could be removed and rotated with the field cage on without damaging any internal components.

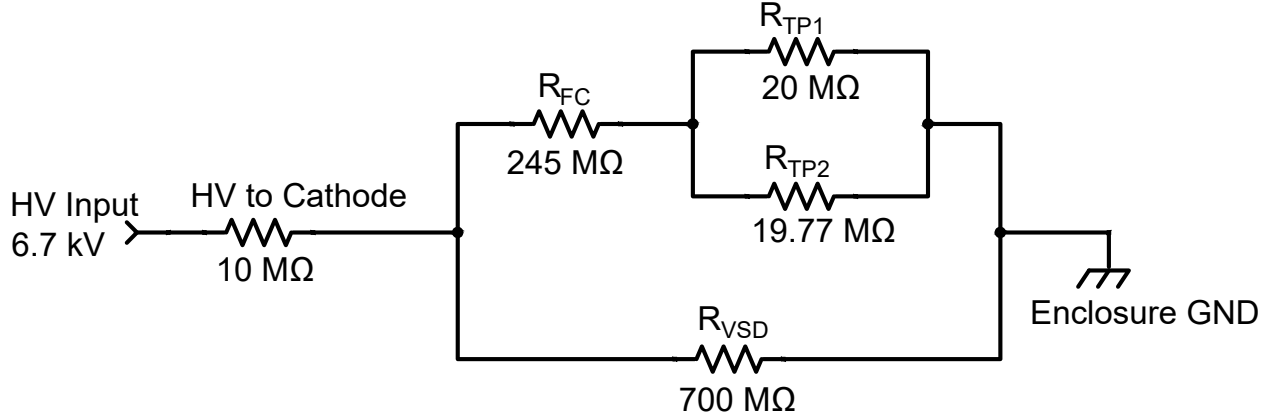


Figure 1.5: Schematic of the TPC system

The cathode is connected to the HV supply through a  $10\text{ M}\Omega$  resistor and has an effective capacitance to ground of  $4\text{ nF}$ ,  $C_{VSD}$ . The cathode voltage  $V_{cath}$  can be calculated from the schematic of the TPC system in Fig. 1.5, as

$$V_{cath} = \frac{V_{HV}}{1 + \frac{10}{((245+R_p)^{-1}+700^{-1})^{-1}}}, \quad (1.1)$$

where

$$R_p = (R_{TP1}^{-1} + R_{TP2}^{-1})^{-1}, \quad (1.2)$$

is the effective resistance of the last resistor, and  $V_{HV}$  is the high voltage supply; all resistor values are given in  $\text{M}\Omega$ .

Figure 1.6 shows a cartoon schematic of the field cage walls. The field cage contains 50 inside copper strips and 49 outside copper strips. The strips on each board were connected to the adjacent strip on the next board; front, back, and side boards were connected by G10 corner pieces with conducting paint strips, creating rings around the whole field cage. The first inside strip is connected to the cathode, which is itself connected by an effective  $5\text{ M}\Omega$  resistor ( $R$ ) to the first outside strip. The first outside strip is connected through a via to the second inside strip, which continues on in this repeating fashion. The resistor chain creates a voltage divider in which each strip is separated by a constant difference voltage at a fixed distance, setting up a constant electric field. The last strip of the field cage is composed of a small inner strip (1.5 mm) on the PCB board and the aluminum

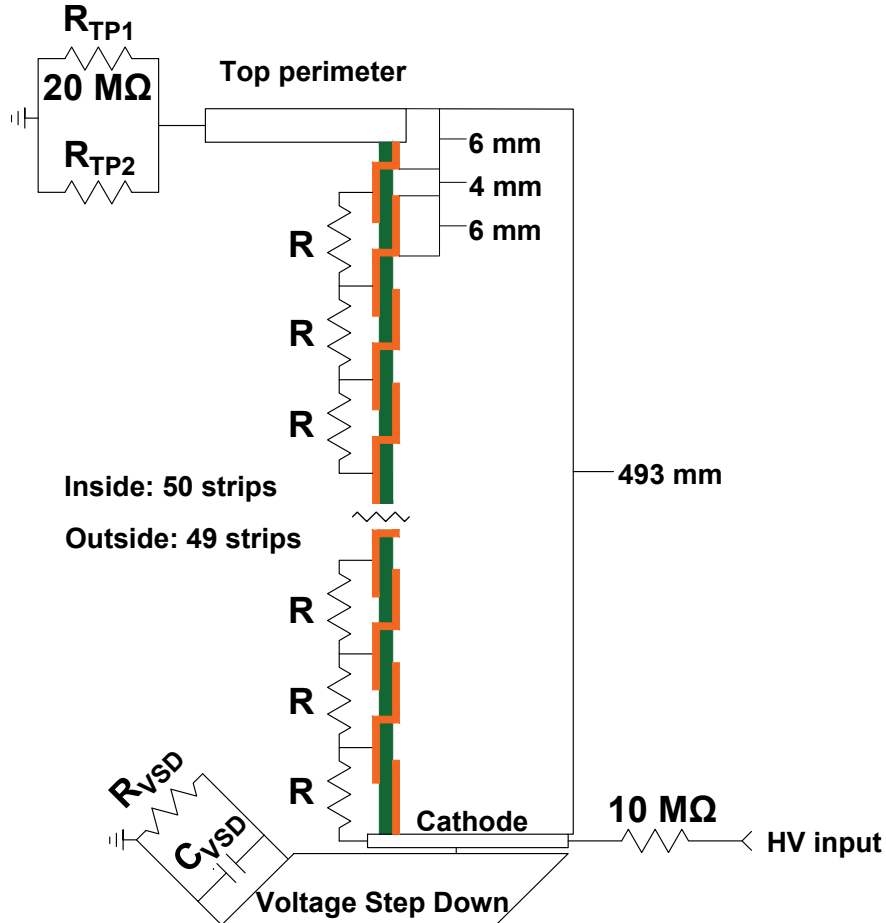


Figure 1.6: Schematic of the electric connections relevant to the Field Cage system. The strip thickness is exaggerated in the figure to show the detail

top perimeter piece (4.5 mm) giving an effective thickness of 6 mm, the same as the other strip widths. The top perimeter is connected to electrical ground through a  $20\text{ M}\Omega$  resistor ( $R_{TP1}$ ) with the option to place an additional resistor ( $R_{TP2}$ ) in parallel to tune the voltage of the top perimeter, as seen in Fig. 1.6.

The voltage on each strip,  $V_n$ , can be expressed as,

$$V_n = V_{cath} \frac{R_p + (50 - n)R}{49 \cdot R + R_p} \quad (1.3)$$

where  $n = 1$  represents the index of the first inside strip, and  $n = 50$  represents the index of the last inside strip, which is the same as the top perimeter voltage.

### 1.2.3 Voltage Step Down

The gap between the field cage's cathode and the ground of the enclosure is quite small. To prevent electric breakdown in the gas between this gap a series of concentric copper rings safely stepped down the voltage to ground; where each ring was separated by a resistor. There were 8 concentric rings with a  $10 \text{ M}\Omega$  resistors in between, creating a resistor chain which steps down the voltage each ring by approximately 1000 V each time. The first ring is the same voltage as the cathode and the last ring is connected to ground. All together the total resistance of the resistor chain is  $700 \text{ M}\Omega$ .

### 1.2.4 Wire Planes

There are three wire planes that are mounted underneath the pad-plane. The wire plane closest to the pad-plane (4 mm) are the anode wires. The next plane (12 mm) is the ground plane or frisch grid, and the last plane (14 mm) is the gating grid. The gating grid is the first plane that electrons meet as they drift upward from the field cage volume towards the anode plane. The gating grid is operated as a gate either allowing electrons and ions through, or blocking them entirely. The ground plane functions to shield the inside volume of the TPC from the high electric field surrounding the anode wires where the avalanche process of the electron takes place. The ground plane is the least interesting plane and is shorted to the enclosure ground by a BNC terminator on the outside of the TPC. If we would like to calibrate the electronics of the TPC we typically inject a pulser into one end of the ground plane and terminate the other end with a  $50 \Omega$  termination.

---

GET electronics settings

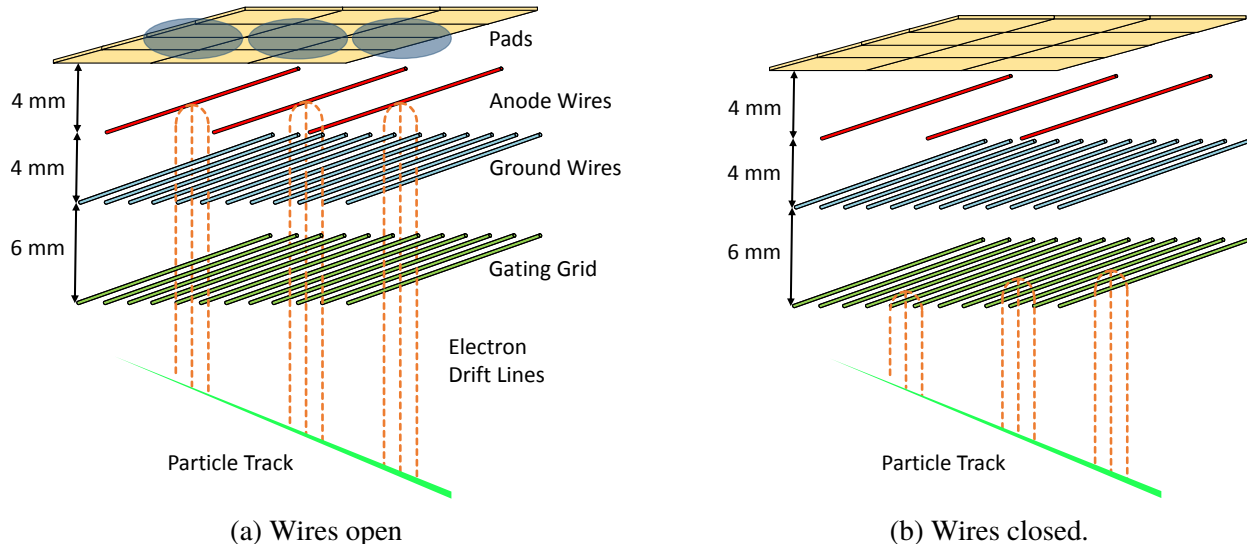
Plane	Material	Diameter $\mu\text{m}$	Pitch mm	Distance to pad-plane	Tension N	Voltage V
Anode	Au-plated W	20	4	4	0.5	1460
Ground	BeCu	75	1	8	1.2	0
Gating	BeCu	75	1	14	1.2	$-110 \pm 70$

Table 1.2: Wire plane properties

In the open configuration the gating grid is transparent to electrons coming from the field cage

volume and also allows for ions to move from the avalanche region into the TPC volume. Typically the gating grid is held in the closed configuration only opening when the data acquisition trigger criteria is met. This is to block the electrons which come from the un-reacted beam, which happens frequently, which if allowed to go to the anode wires, would quickly build up enormous amounts of positive ions and flood the volume of the field cage with space charge. We close the gating grid after reading out approximately one TPC volume – about  $10\text{ }\mu\text{s}$  – to also prevent the back-flow of ions from the avalanche region from that event. Since ions move with a velocity much slower than that of electrons, the ions only move several  $\mu\text{m}$  in the time the gate is open; this allows for electrons to pass through while preventing the back-flow of ions into the FC volume.

Figure 1.8 shows a Garfield simulation of the gating grid in both the on and off configurations. In the on configuration, all the wires share the same average voltage,  $V_{g.g.}$ , which is optimized for the case of 100% electron transparency. In the off configuration, the reference voltage  $V_{g.g.}$  remains the same, but alternating wires get an offset voltage of  $\pm\Delta V$ , so that the electric field produced by the voltage difference  $2\Delta V$  between wires is great enough to block incoming electrons. Opening the grid from this closed bi-polar mode is simply done by removing the offset voltage and allowing the two wires to short which equilibrates their charges, which is the state of the reference voltage.



Both configurations of the gating grid were measured and simulated. To measure the electron

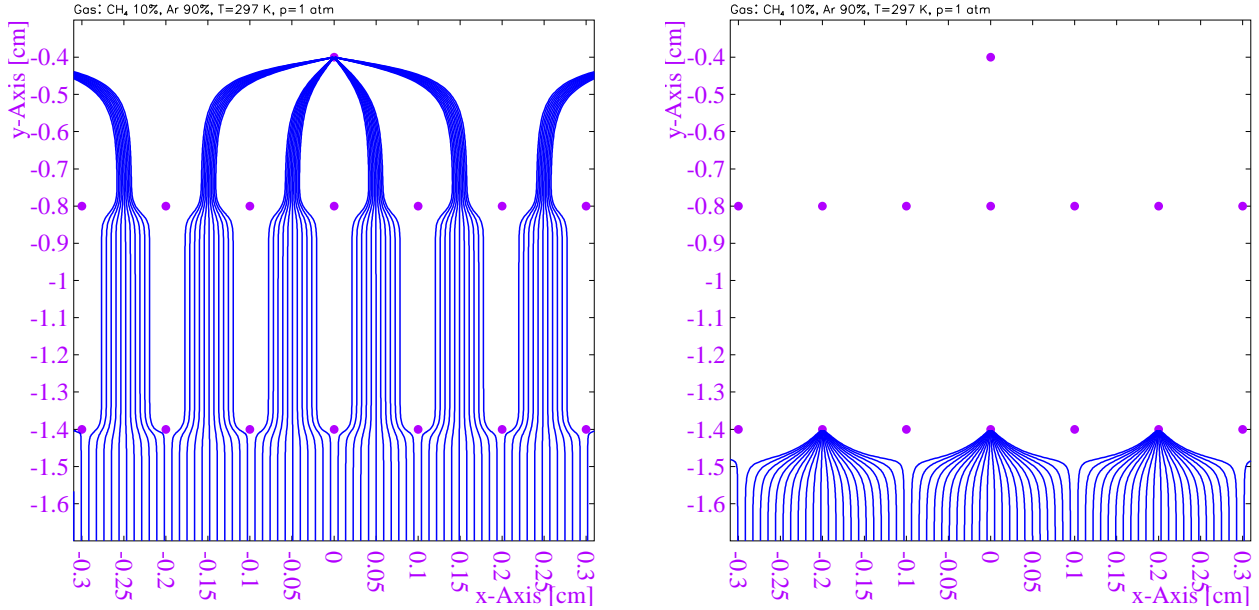
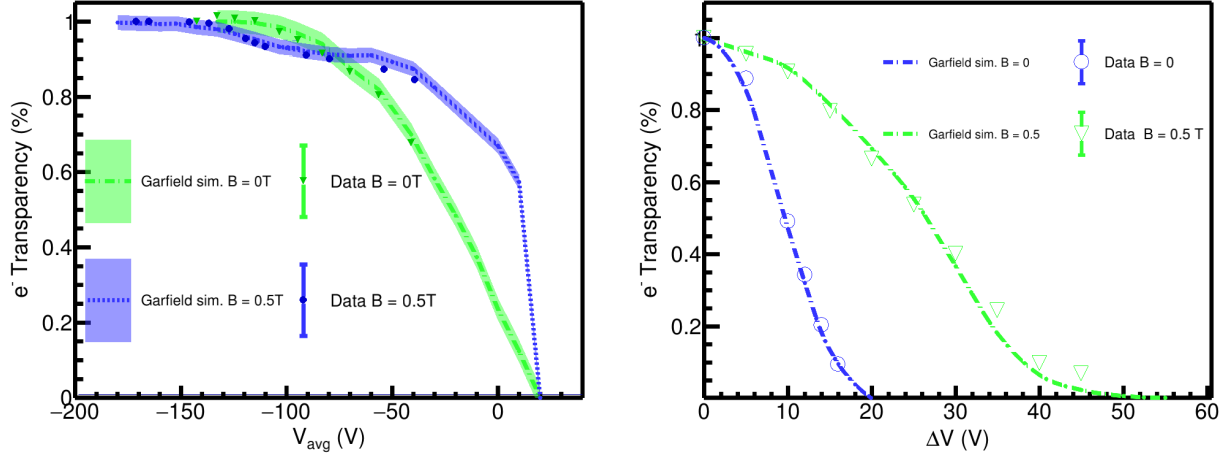


Figure 1.8: On and off configurations of the gating grid.

transparency were all wires share the voltage  $V_{avg}$ , the anode wire was lowered to 500 V and the beam was allowed to enter the field cage without any target put in. By lowering the voltage of the anode we could measure the large charge of the beam without saturating the electronics. The average charge deposited in the chamber could be measured as a function of  $V_{avg}$ ; changing the top plane resistor appropriately according to Eq. 1.6. Several runs were taken ranging from  $-198$  V to  $-40$  V, with and without the magnetic field. Theoretically the most negative value represents 100% electron transparency and was used as the reference run. The electron transparency,  $T$ , was defined as  $T = \langle dE/dx \rangle / \langle dE/dx \rangle_{ref}$ , where  $\langle dE/dx \rangle_{ref}$  represents the average energy loss of the reference run. Figure 1.9a shows the measured transparency as a function of  $V_{avg}$ , as compared with the corresponding Garfield simulation. The average gating grid voltage used in the experiment was  $-171$  V to ensure we were well within the 100% transparency region.

To measure the electron transparency as a function of the difference voltage  $\Delta V$ , the average voltage was first set to 100% transparency,  $V_{avg} = -171$  V, and the difference voltage was added or subtracted from alternating wires. Figure 1.9b shows the result of the simulation and experiment with and without the magnetic field. By introducing the magnetic field the required voltage to close

the grid increases. In the experiment we selected the value of  $\Delta V = 65$  V to ensure we were well within the region of 0% transparency.



(a) Electron transparency for the conditions of all wires are the same voltage.  
(b) Electrons transparency for the mode where adjacent wires have a voltage difference of  $2\Delta V$ .

The anode wires are typically biased to  $10^3$  V and are very thin, about 20  $\mu\text{m}$  in diameter. This creates a very high electric field very close to the anode wire in which the electron gains kinetic energy producing electrons until it terminates on the anode wire or the pad plane. The amount of electrons it produces depends on the anode wire voltage and the gas properties. The absolute gas gain was not experimentally measured but was simulated by a Garfield simulation. During the experiment the anode wires were biased to two different voltages. We will refer to the voltage 1460 V as the “high voltage” and 1214 V as the “low voltage”. Only two sections were biased with the lower voltage setting due to concerns of a high current issue. Figure 1.10 shows the expected number of electrons distributions for electrons produced in a avalanche process of an electron creating a single avalanche. The distribution follows the expected Polya distribution and the MC data in the simulation was fit with a Polya function [4].

The wire plane and the cathode define the different electric field regions. The main drift region is defined by the space between the gating grid and cathode voltages (Region 1), with a small drift region being defined by the space between the ground grid and the gating grid (Region 2); the avalanche region is defined as between the ground grid and the anode grid. The voltage of the

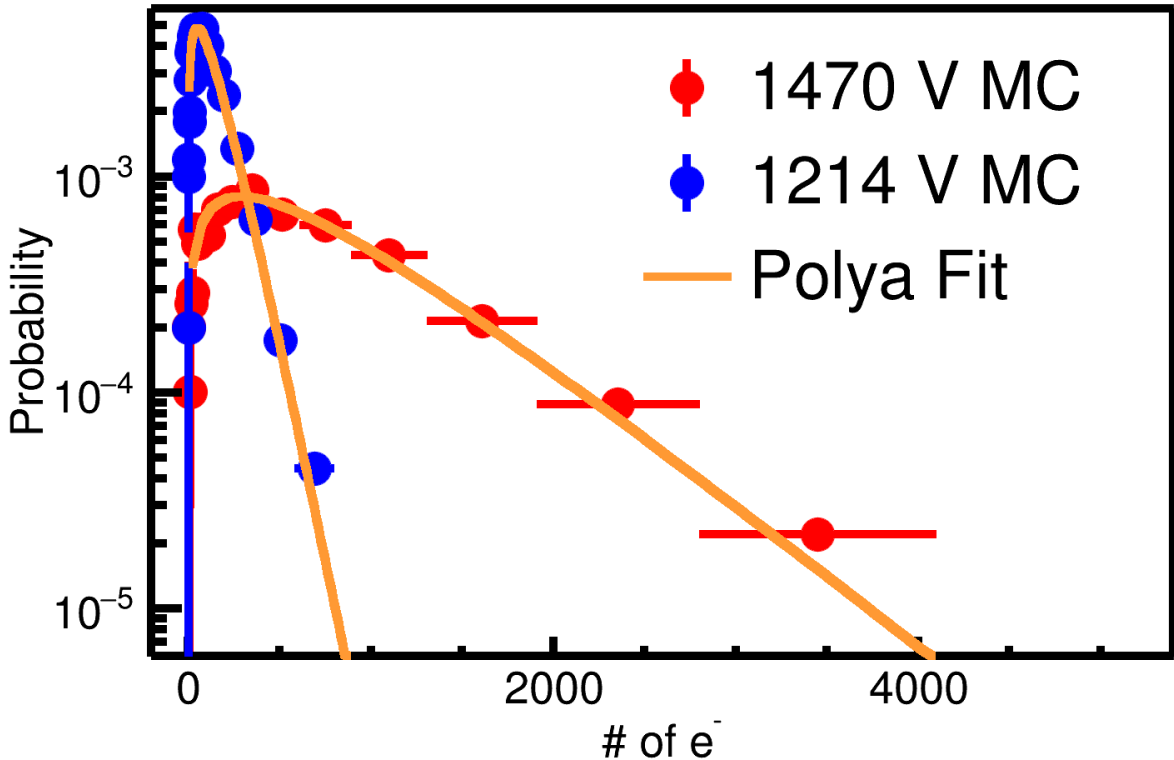


Figure 1.10: Number of electrons produced in a single avalanche on an anode wire. Two different voltages were simulated using Garfield++ at 1470 V and 1214 V. The expected Polya distribution fit is also given in yellow.

gating grid is set to the point that allows for 100% transparency for electrons. It is possible that the electric field in Region 1 and Region 2 can be matched but not required. The voltage of the top perimeter is set by adjusting the value of the last resistor ( $R_{TP2}$ ) to ensure the electric field is constant through Region 1. We can imagine Region 1 is split into two virtual volumes, one defined between the cathode and the top perimeter, and one defined between the top perimeter and the gating grid. The magnitude of the electric field in the region between the top perimeter and the cathode,  $E_1$ , is defined as,

$$E_1 = \frac{V_{g.g.} - V_{tp}}{y_{g.g.} - y_{tp}}, \quad (1.4)$$

where  $V_{g.g.}$ ,  $V_{tp}$ ,  $y_{g.g.}$ , and  $y_{tp}$  are the voltage and vertical y-position of the gating grid and top perimeter respectively. The magnitude of the electric field in the region between the top perimeter

and the cathode,  $E_2$ , is defined as,

$$E_2 = \frac{V_{tp} - V_{cath}}{y_{tp} - y_{cath}}, \quad (1.5)$$

where  $V_{tp}$ ,  $V_{cath}$ ,  $y_{tp}$ , and  $y_{cath}$  are the voltage and vertical y-position of the top perimeter and cathode respectively. The condition for a smooth electric field across the volume is given by  $E_1 = E_2$ . Substituting Eq. 1.3 for  $V_{tp}$  ( $n = 50$ ), we can solve for the effective resistance of the top perimeter  $R_p$  as,

$$R_p = 49 \cdot R \left( \frac{\frac{y_{g.g.} - y_{cath}}{y_{TP} - y_{cath}} - 1}{\frac{V_{cath} - V_{gg}}{V_{cath}}} \right), \quad (1.6)$$

where the relevant vertical dimensions are  $y_{g.g.} - y_{cath} = 497.3$  mm and  $y_{tp} - y_{cath} = 490$  mm.

The value of  $R_{TP2}$  can be calculated from Eq. 1.2 and Eq. 1.6.

### 1.2.5 Pad Plane

The pad-plane is a multi-layer circuit board which is segmented into 11.5 mm x 7.5 mm charge sensitive pads; arranged in an array of 108 x 112 pads in the x and z-directions respectively making 12096 pads in total. There is an insulating gap of 0.5 mm on each side separating the pads. The effective area covered by the pads is 1344 mm x 864 mm. There is a via and trace coming from each pad to the opposite side of the pad plane and is arranged in a surface pads which may be readout by a surface mount SAMTEC connector CITE HERE. Add figure of close up of pad plane

### 1.2.6 Electronics

Signals in the S $\pi$ RIT TPC are amplified and digitized by the recently developed Generic Electronics for TPCs (GET) [5]. Short cables transmit the signals from the pads to the inputs of the AGET chips. Each AGET chip services 64 pads (63 pads are connected in our case), contains a pre-amplifier, and a Switched Capacitor Array (SCA), with a maximum of 512 time buckets with an adjustable sampling frequency of 1 to 100 MHz. Four AGET chips are mounted on one AsAd (ASIC and

---

GET electronics settings	
ADC bit range	14 bits
Sampling frequency	1-100 MHz
Dynamic range	.12, .24, 1.0, 10pC
Peaking time	69,117,232,501,720,1014 ns
Time bucket range	512

---

Table 1.3: Summary of range of GET electronics settings.

ADC) motherboard. The gain of each AGET can be configured as 0.12, 0.24, 1.0, or 10 pC over the whole dynamic range, and the ADCs on each AsAd board provides 12 bit resolution. The peaking times of the shaping amplifiers can be set to 69, 117, 232, 501, 720, or 1014 ns. In this experiment, the gain was set to the highest setting, 0.12 pC, the peaking time 117 ns, and the sampling frequency 25 MHz (resulting in 40 ns time buckets). The Aget 2.0, asad 2.1, and cobo 1.0 firmware versions were used. The variations in the electronics were calibrated by measuring the response of each channel to a injected reference pulse, covering the full dynamic range of each channel.

### 1.3 Energy loss in material

The average energy loss in a material can be described by the Bethe-Bloch equation,

$$\frac{dE}{dx} = \frac{4\pi N Z^2 e^4}{mc^2 \beta^2} \left( \ln \frac{2mc^2 \beta^2 \gamma^2}{I} - \beta^2 \right). \quad (1.7)$$

Where  $N$  is the number density of electrons in the medium,  $e$  the elementary charge,  $mc^2$  is the rest mass of the electron,  $Z$  is the charge of the traversing particle,  $I$  is the mean excitation energy of the medium, and  $\beta$  is the velocity of the particle. There is a large variation in energy loss around this mean value, with a long high energy loss tail.

The statistical variation of energy loss in a material was described by Landau [6] and later better described by Shulek [7] and Bichsel [8]. In both approximations it is described by a most probable energy loss value with a long, high-energy loss tail. Because of this long tail, for a finite set of energy loss measurements along a given track, the fluctuation of the mean value energy loss is a

very unreliable observable. The most probable energy loss is the most desirable observable either through fitting of the observed distribution or through the truncated mean method. The truncated mean is the average mean value calculated after throwing away the top fraction of the highest energy loss entries, where the fraction used in this thesis was 30%. This approximates the most probable value without performing a fit to a known distribution. There are

A full description of the energy loss distribution can be described in CITE HERE.

### 1.3.1 Gas Properties

The gas contained by the field cage was a mixture of 90% Ar and 10% Methane ( $\text{CH}_4$ ) by volume (P10 gas), and operated just under atmospheric pressure (1 atm). The gas was continually flowed through the field cage and exited into the enclosure volume, finally passing through a bubbler to atmosphere. The gas purity was monitored with an oxygen and water monitor which are the two most concerning contaminants. The water never exceed ??? ppm and the oxygen level never exceeded ??? ppm. Figure 1.11 shows the drift velocity of P10 gas at 1 atm (760 Torr) as a function of the reduced electric field value given in units of  $\text{V cm}^{-1} \text{ Torr}^{-1}$ . Operating near the peak value of the drift velocity curve minimizes the change in the drift velocity as the effective field slightly changes due to slight variations in the pressure. The electric field in the experiment was  $125 \text{ V cm}^{-1}$  at 760 Torr, giving a reduced electric field  $0.17 \text{ V cm}^{-1} \text{ Torr}^{-1}$ .

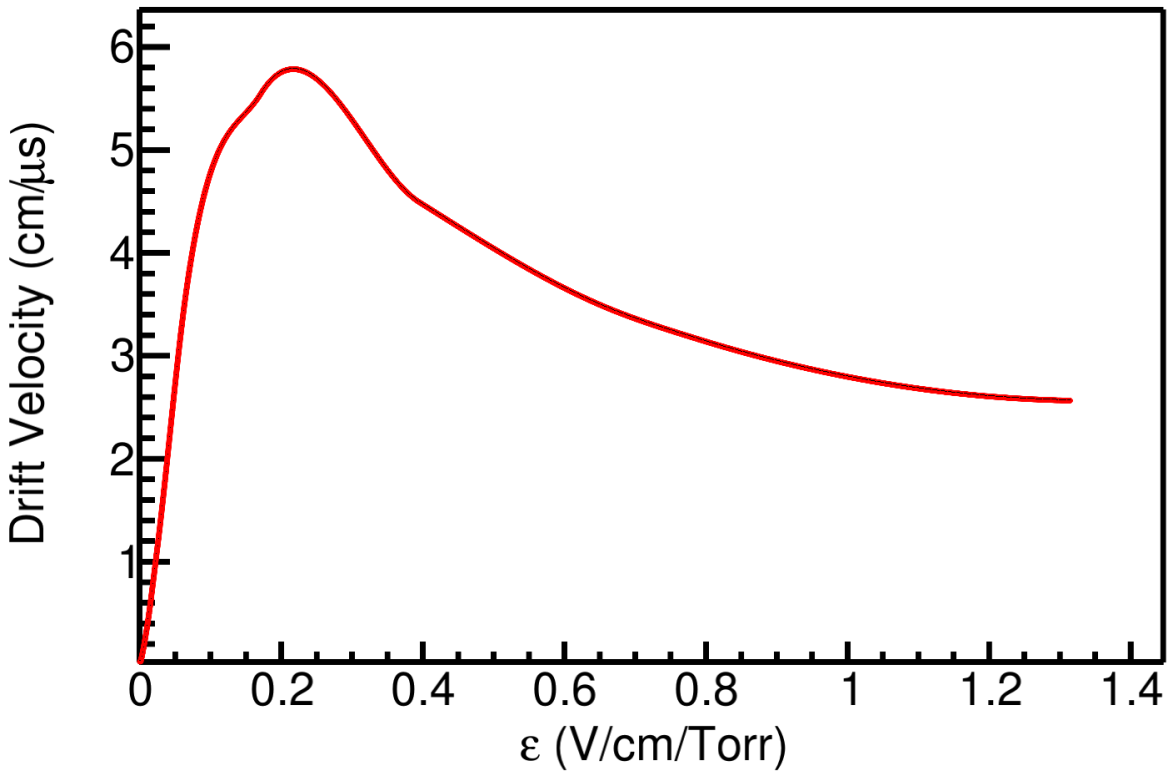


Figure 1.11: Drift velocity of electrons in P10 gas.

The general formula for the drift velocity,  $d\vec{x}/dt$ , of an electron in the presence of electric and magnetic fields,  $\vec{E}$  and  $\vec{B}$ , can be expressed in the Langevin equation as,

$$\frac{d\vec{x}}{dt} = \frac{\mu}{1 + (\omega\tau)^2} \left( \vec{E} + \omega\tau \frac{\vec{E} \times \vec{B}}{|\vec{B}|} + \omega^2\tau^2 \frac{\vec{E} \cdot \vec{B}}{|\vec{B}|^2} \vec{B} \right), \quad (1.8)$$

where  $\mu$  is the signed drift velocity,  $\omega$  is the cyclotron frequency, and  $\tau$  is the collision parameter for a particular gas [4].

Several properties of the gas were also simulated in Garfield such as the longitudinal and transverse diffusion,  $\sigma_l$  and  $\sigma_t$  respectively, and the electron and ion drift velocities,  $v_d$  and  $v_i$  respectively for the experimental electric field of  $125 \text{ V cm}^{-1}$ ; summarized in Table 1.4.

Gas properties	$\sigma_t$ (cm $^{-1/2}$ )	$\sigma_l$ (cm $^{-1/2}$ )	$v_d$ (cm $\mu$ s $^{-1}$ )	$v_i$ (cm $\mu$ s $^{-1}$ )	$G_h$	$G_l$
	0.024	0.034	5.43	$2.05 \times 10^{-4}$	903	150

Table 1.4

## 1.4 Pad Response Function

Each electron avalanche produces an two-dimensional image charge on the pad plane, as shown in the cartoon in Fig. 1.12, where the projection of the charge distribution onto the  $x$  and  $z$  axis of this distribution are labeled as  $\rho(x)$  and  $\rho(z)$  respectively. If  $\rho(x, z)$  represents the charge distribution on the pad-plane, the total charge observed on each pad,  $Q$ , is given as,

$$Q(x_o, z_o) = \int_{z_o - \frac{l}{2}}^{z_o + \frac{l}{2}} \int_{x_o - \frac{w}{2}}^{x_o + \frac{w}{2}} \rho(x, z) dx dz, \quad (1.9)$$

where  $x_o$  and  $z_o$  represent the  $x$  and  $z$  coordinates of the center of each pad,  $w$  is the width, and  $l$  is the length. This function is commonly referred to as the Pad Response Function (PRF). The total charge observed for this track is a superposition of PRFs of each avalanches on all the anode wires. It is the use of this PRF that allows for sub-millimeter accuracy in the position resolution of the TPC [4]. Typically in a TPC, hits are grouped into clusters and it is practical to cluster in only one direction. The PRF can be expressed in a way that is independent of the location of the avalanche. If the true position of the avalanche is  $(x'_o, z'_o)$ , and the charge distribution can be written in a position independent way

$$Q(\lambda_x) = \int_{z_o - \frac{l}{2}}^{z_o + \frac{l}{2}} \int_{x_o - \frac{w}{2}}^{x_o + \frac{w}{2}} \rho(\lambda_x, \lambda_z) dx dz, \quad (1.10)$$

and the PRF for row clustering can be written as,

$$Q(\lambda_z) = \int_{z_o - \frac{l}{2}}^{z_o + \frac{l}{2}} \int_{x_o - \frac{w}{2}}^{x_o + \frac{w}{2}} \rho(\lambda_x, \lambda_z) dx dz. \quad (1.11)$$

The direction most perpendicular to the track's direction of travel provides the most accurate position resolution. Clustering in the S $\pi$ RIT TPC is done for several pads containing charge in the direction most perpendicular to the track's direction of travel.

In this example the clustering direction would be along the  $x$  axis, as illustrated by the bolded pads. By choosing to cluster only in one direction, we have not included the charge in adjacent pads along the  $z$  axis resulting from the tails of  $\rho(z)$ . Therefore the charge not included in the bolded pads will be incorporated into adjacent clusters, introducing small correlations in charge between neighboring clusters.

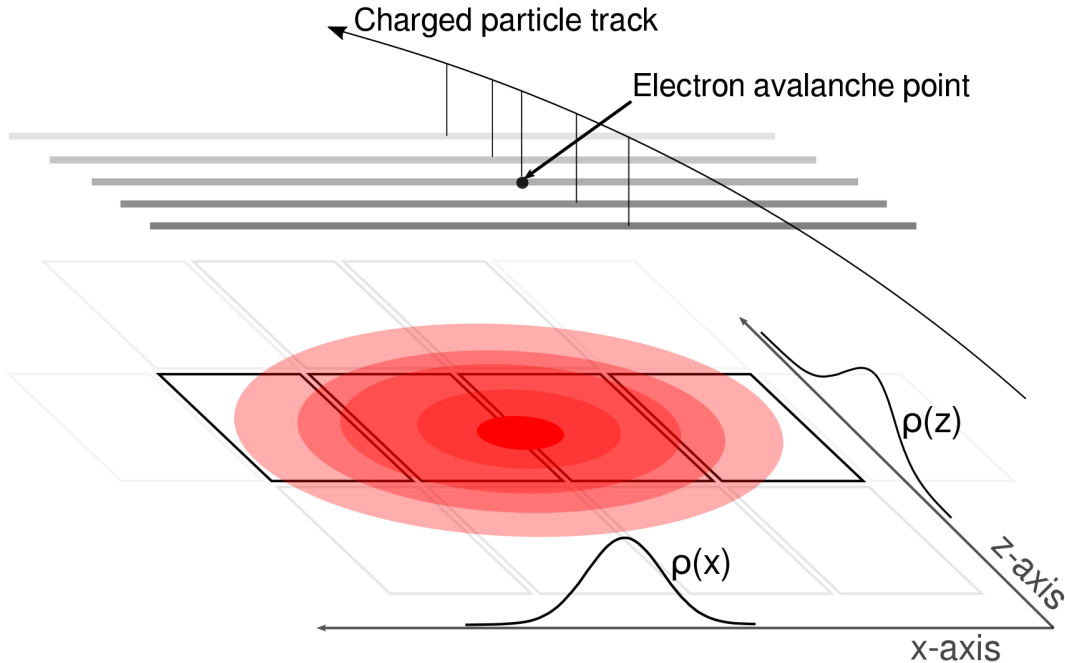


Figure 1.12: A cartoon illustration of the charge distribution resulting from an electron avalanche on one wire and the projections of the distribution onto the two axis  $\rho(x)$  onto the x-axis and  $\rho(z)$  onto the z-axis. The orientation of the wire planes is flipped upside down to display the perspective better.

Gatti [9] derived a semi-empirical formula for the charge distribution in a simple multi-wire TPC given as,

$$PRF_{\text{Gatti}}(\lambda) = \frac{K_1}{K_2 \sqrt{K_3}} [\arctan(\sqrt{K_3} \tanh[K_2(\frac{\lambda}{h} + \frac{w}{2h})]) - \arctan(\sqrt{K_3} \tanh[K_2(\frac{\lambda}{h} - \frac{w}{2h})])] \quad (1.12)$$

where  $w$  is the width of the pad,  $h$  is the distance of the anode plane to the pad plane, and  $\lambda$  is the distance of the pad center to the avalanche point. It is a single parameter equation where the two parameters  $K_1 = \frac{K_2\sqrt{K_3}}{4\arctan(\sqrt{K_3})}$  and  $K_2 = \frac{\pi}{2} \left(1 - \frac{\sqrt{K_3}}{2}\right)$  depend on the parameter  $K_3$ , which is a function of the ratio of the anode wire diameter to the distance of the anode wires to the pad plane.  $K_3$  can be looked up in a graph in [4] and [9].

### 1.4.1 Experimental Pad Response Function

The correlations we introduced by only clustering along one direction do not play a significant role in the particle identification, but cause deviations from the expected Gatti distribution. Also, analytic PRFs only exist for classical multi-wire TPCs. For these reasons it is useful to experimentally measure the PRF and fit it with an empirical function, typically a Gaussian, to describe its behavior.

As in Fig. ??, we postulate that the PRF is a function of the total charge deposited in a cluster  $Q = \sum_i q_i$ , and the difference in position of the center of the  $i^{th}$  pad,  $x_i$ , to the mean position  $\bar{x} = \sum_i x_i q_i / Q$ , defined as  $\lambda_i = x_i - \bar{x}$ . The PRF is simply defined as the charge fraction of each pad as a function of  $\lambda$ , as shown in Equation 1.13.

$$PRF(\lambda_i) = \frac{q_i(\lambda_i)}{Q} \quad (1.13)$$

Averaging over many events in the experimental data, the resulting PRF for the S $\pi$ RIT TPC is shown in Fig. 1.13. Here we see the deviations from the expected analytic Gatti distribution (black curve), whereas fitting with a two parameter Gaussian function (red curve) gives a better description of the data, Eq. 1.14, with the two parameters being the normalization coefficient,  $N_0$ , width  $\sigma$ , and with a mean value assumed to be 0.

$$PRF_{\text{Gaus}}(\lambda) = N_0 e^{\frac{-\lambda^2}{2\sigma^2}} \quad (1.14)$$

The shape of the PRF depends on the crossing angle of the track [9]. Plotted in Fig. 1.14 is the PRF of  $\pi^-$  tracks vs. the crossing angle  $\theta$ . The PRF gets wider starting from  $90^\circ$  and going to

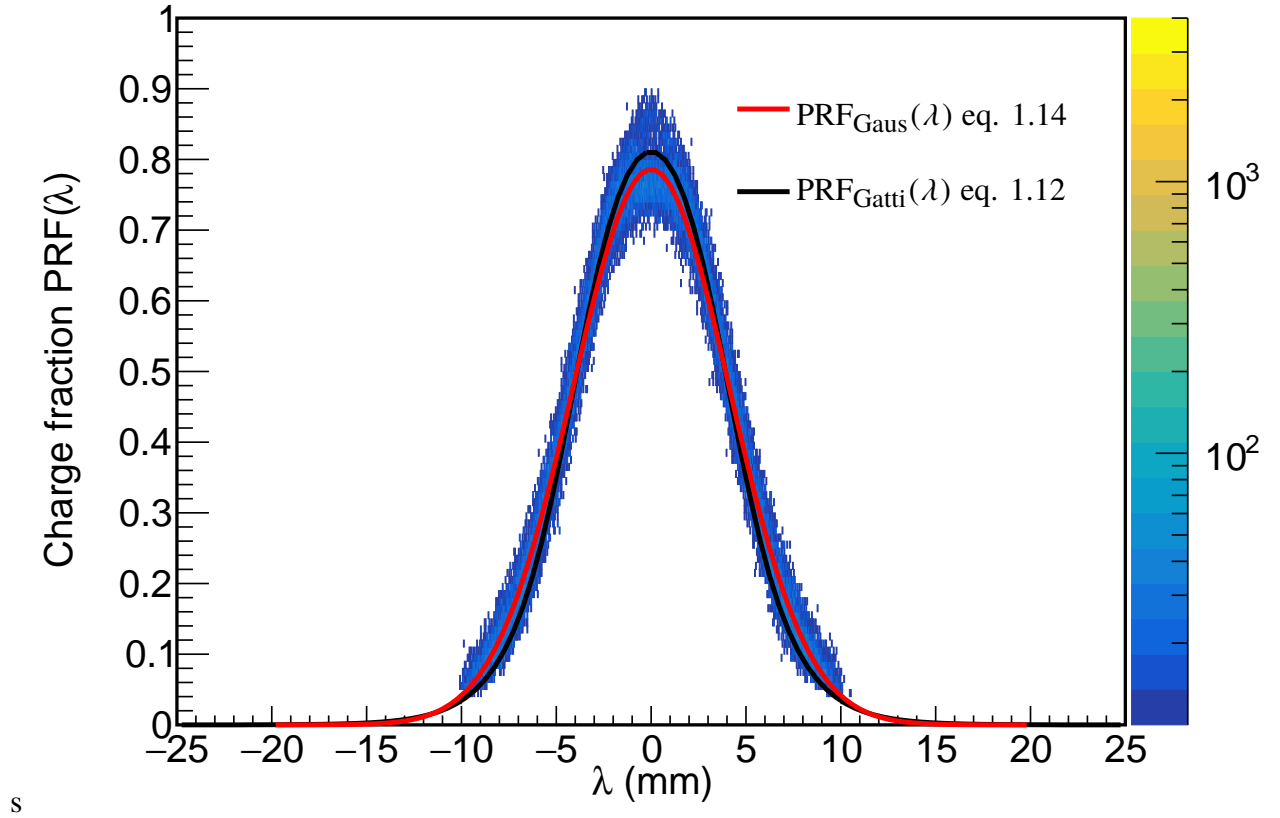


Figure 1.13: Experimental pad response function of many events for a crossing angle of  $85^\circ < \theta \leq 90^\circ$ .

$45^\circ$ ; if we did not switch clustering directions the PRF would become wider until it was a uniform distribution and there was no position resolution. Since we switch the clustering direction from  $x$  to the  $z$  direction at  $45^\circ$ , the opposite trend is seen where the PRF becomes narrower as the position resolution gets better going from  $45^\circ$  to  $0^\circ$ .

Fits were performed to the experimental data with  $5^\circ$  width bins from  $0^\circ < \theta \leq 90^\circ$ . The two parameters of the Gaussian fits are plotted versus  $\theta$  in Fig. 1.15; a  $4^{th}$  order polynomial fit between these points allowed for interpolating between  $\theta$ .

#### 1.4.2 Considerations when constructing a TPC

Several considerations went into the construction of the S $\pi$ RI TPC which I wish to summarize and document here. All materials and glues of the TPC were selected as low out-gassing materials.

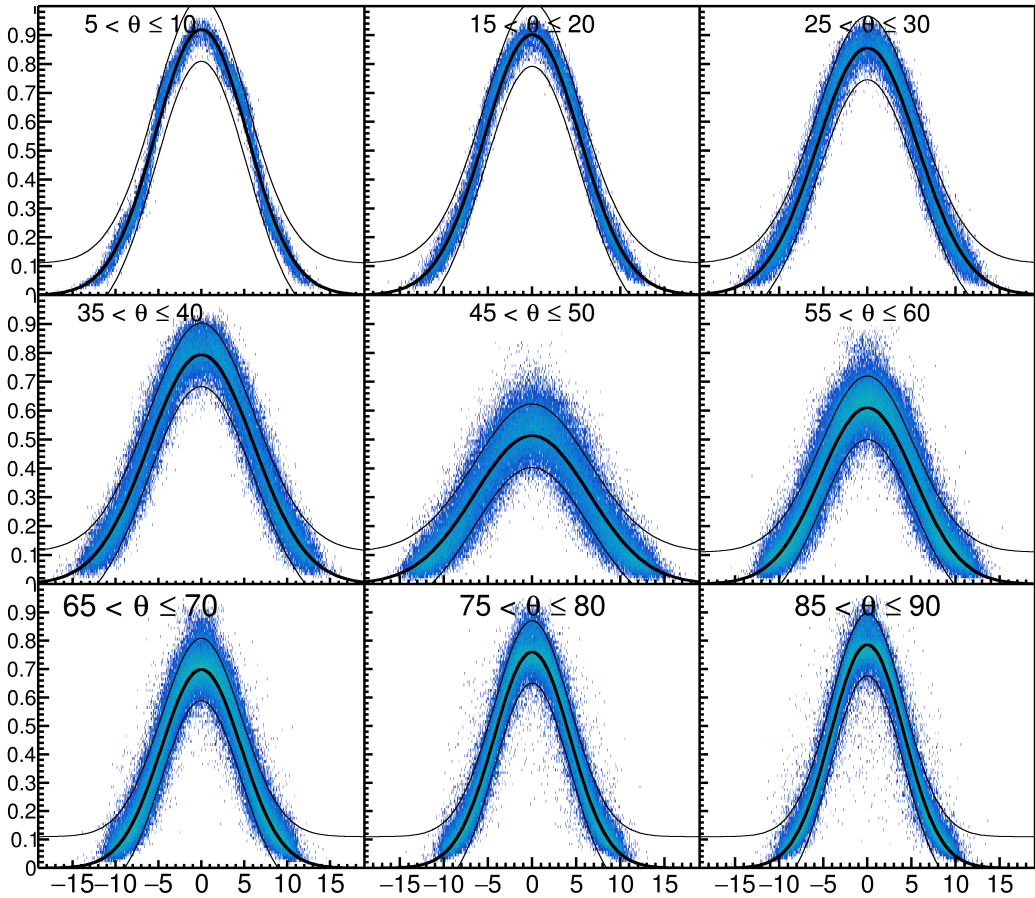


Figure 1.14: PRF response from  $\pi^-$  data.

Several materials (that are common place in nuclear labs), such as vacuum grease, viton o-rings, all out-gas organic chemicals into the counter gas which damage the TPC by permanently lowering the gain over time. The organic molecules responsible are difficult to identify exactly, but lists of good and bad materials are well known in the literature from experiments. If a material we wished to used was not on these lists we placed the material in a clean chamber with the counter gas and flowed this counter gas through a small proportional counter making sure the gain did not drop at high collection rates when exposed to a high rate alpha Americium source.

Sparking Two volumes of gas.

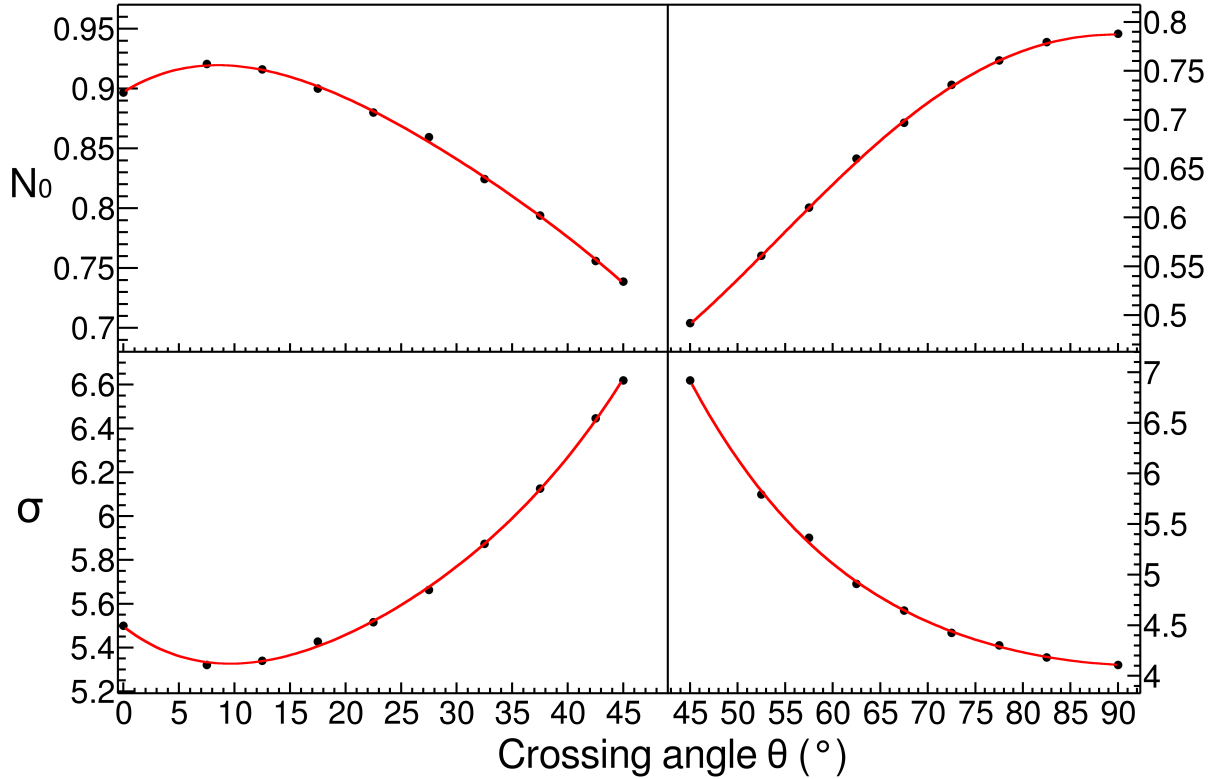


Figure 1.15: Parameters  $N_0$  and  $\sigma$  as a function of the crossing angle  $\theta$  with the 4<sup>th</sup> order polynomial fits.

## 1.5 Ancillary Detectors

### 1.5.1 Kyoto Multiplicity Trigger

The Kyoto Multiplicity Array consists of two arrays of plastic scintillating bars on each side of the TPC, each consisting of 30 bars. The entire TPC structure was designed so that light charged particles could easily pass through the field cage and side walls of the TPC enclosure. In this way the number of tracks passing through the sides of the TPC could be measured by this array. In heavy ion collisions the more central a nuclear collision is, the more nucleons participate in the collision, resulting in more measured tracks. It is this correlation between the number of tracks and centrality of the collision that makes the Kyoto Array sensitive to the centrality of events. It is more likely that in very central collisions more tracks are going to the peripheral angles and measured

by the Kyoto array. In the experiment the trigger selection criteria was  $n_{Kyoto} > 4$ , where  $n_{Kyoto}$  is the total number of tracks measured by both arrays.

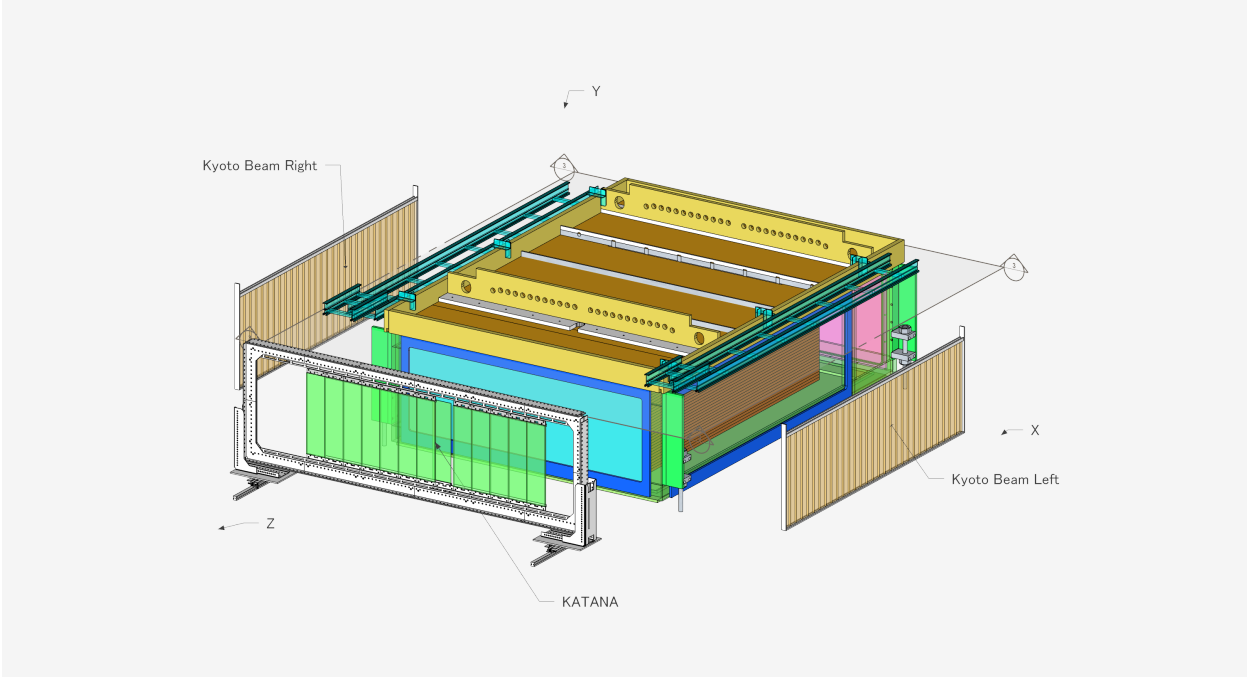


Figure 1.16: Exploded views of Kyoto and KATANA arrays.

### 1.5.2 Krakow KATANA Veto and Multiplicity Array

The Krakow KATANA array consists of 12 plastic scintillating bars mounted to the downstream wall of the TPC enclosure. Three of the 12 bars were thin and operated as a beam veto in the event the beam did not make a nuclear collision with the target; this was a majority of the time. The 9 other bars operated as an additional multiplicity array similar to the Kyoto array. Since most of the particles are focus forward in a cone in the laboratory frame, it was found the condition on the Kyoto array was sufficient to trigger on central events; thus the KATANA array was used in primarily the beam veto mode. This was accomplished by positioning the array so that the expected position of the beam exiting the TPC would be centered on the three thin paddles. The threshold of the veto paddles were set so that the charge of a particle,  $Z$ , was  $Z > 20$ . This allowed the selection of very

central events and we did not trigger on very peripheral or no collision events.

### 1.5.3 Active Veto Array

The beam was tuned by two sets of quadrupole magnets, STQ 1 and STQ2, so that the beam spot was focused on the TPC target location. Because of the inherent angular dispersion of the beam there were incoming beam events which significantly deviated from the target location. To veto these type of events an active veto array was set at the entrance of the TPC consisting of four small scintillating bars arranged to be slightly larger than the target size. The threshold was set so that any beam particle which passed through any of the bars it would send a trigger signal to not trigger the system since the beam path would not be on target but on some other material inside the TPC.

## 1.6 Radio Isotope Beam Factory (RIBF) Facility

The primary and secondary beams were produced at the Radioactive Isotope Beam Factory (RIFB) facility at RIKEN, in Wako-shi, Japan. The RIBF facility starts with two primary beam types,  $^{132}\text{Xe}$  and  $^{238}\text{U}$ , which produced by an ion-source and accelerated to progressively higher kinetic energies by 1 linear accelerator (RILAC), and 4 different cyclotrons (RRC, fRC, IRC, and SRC), reaching a primary beam energy of 345 MeVA.

After the SCR, the primary beams impinge on a rotating 3 mm Be target which produces many different species by fragmentation. These fragments are then separated by the BigRIPS spectrometer which is tuned to the particular secondary fragment of interest. This is accomplished through several dipole magnets, slits, and wedge degraders. The resulting secondary beam is not pure and the purity depends on the primary beam and target beam desired.

In these set of experiments several beams were produced with varying intensities and purities. Table 1.5 summarizes the average qualities of the 4 secondary beams produced in the two experimental campaigns.

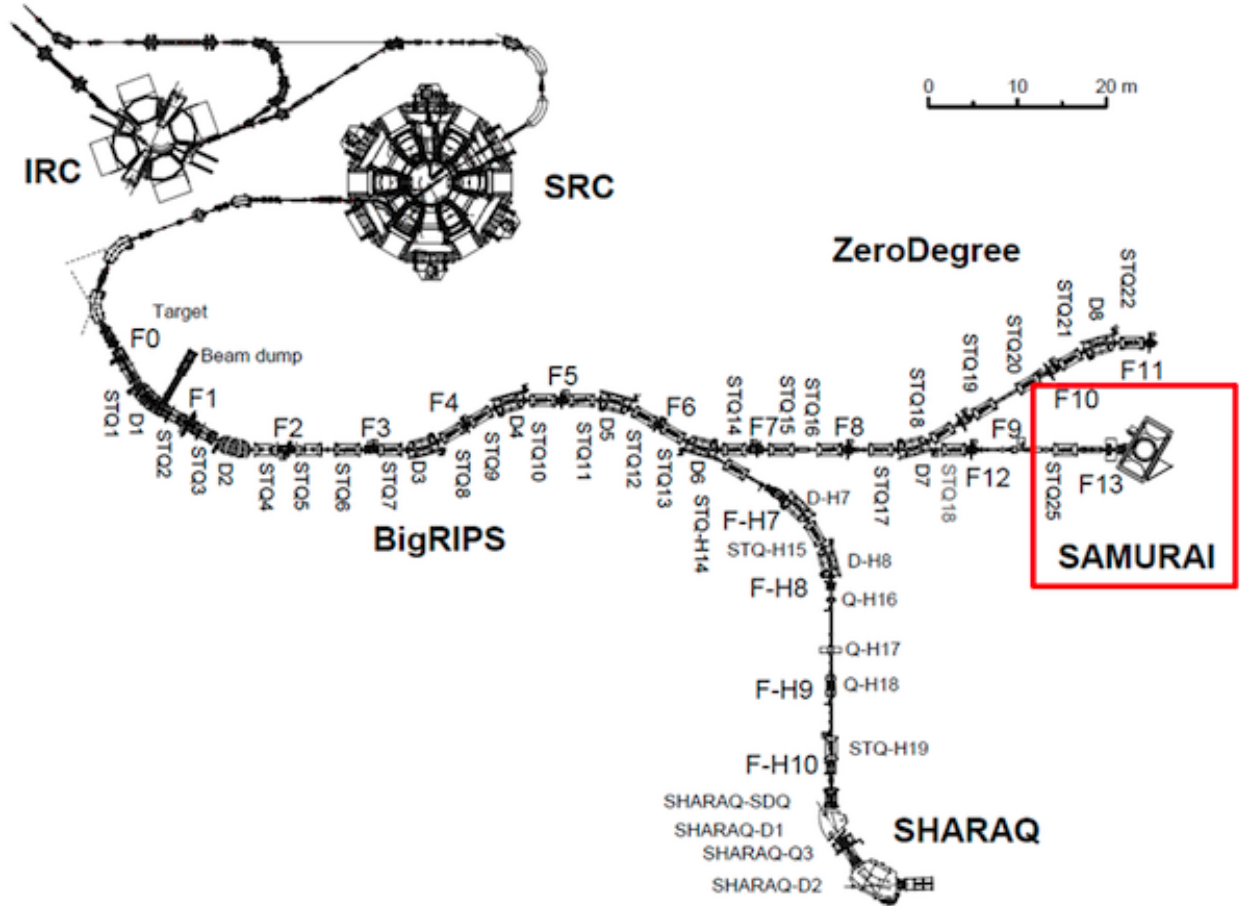


Figure 1.17: Overview of the RIBF, BigRIPS, and SAMURAI beamline.

## 1.7 Experimental Setup

The S $\pi$ RIT TPC was designed to fit exactly into the dipole gap of the dipole magnet at the end of the BigRIPS beam line. Figure 1.18 shows a drawing of the S $\pi$ RIT TPC inside of the SAMURAI magnet chamber which was rotated to the 0° configuration. Typically the SAMURAI (Superconducting Analyzer for Multi-particles from Radioisotope beams) is operated under vacuum as a large-acceptance multi-particle spectrometer for radioactive-beam experiments. This magnet can reach magnetic fields up to 3 T at the center of the pole gap. The space between the magnetic pole faces is further complicated by large bolts which protrude from the pole faces. These bolts secure the vacuum chamber to the magnet which is not practically removable; though the inside of the magnet was not operated under vacuum. This required an extensive rail system and support

Primary Beam	Secondary Beam	Energy at mid target MeVA	Intensity kHz	Purity (%)
$^{238}\text{U}$	$^{132}\text{Sn}$	269.2	9.5	54
$^{238}\text{U}$	$^{124}\text{Sn}$	270.3	9.1	10
$^{124}\text{Xe}$	$^{112}\text{Sn}$	270.4	7.6	48
$^{124}\text{Xe}$	$^{108}\text{Sn}$	269.3	7.5	52

Table 1.5: Primary and secondary beam properties produced in the S $\pi$ RIT TPC experimental campaigns.

frame to slowly slide in the TPC over the bolts, finally raising the TPC several cm to the final height.

The height of the TPC was roughly aligned with a self-leveling laser system to match the center of target with the center of the beam line. Once the TPC was adjusted to the final location, the position of the TPC was measured in fine detail with a photogrammetry system CITE HERE. Small highly reflective targets were placed all over the TPC both inside and out and pictures were taken with a calibrated lens and camera system. Using the commercial software provided the set of different camera perspectives reconstruct a point cloud of all the targets into 3-dimensional coordinates. Since the magnet was also measured with the same system after installation, we can match the two systems to get the absolute position of the TPC – and several of its internal components– relative to the magnet frame. The position resolution of this type of system was estimated to be around 200  $\mu\text{m}$  for each coordinate, which is much more precise than needed CITE HERE or Show data.

Maybe put a position table summary here of the TPC position and definition of the coordinates system in the TPC frame and the Magnet frame

## 1.8 Data Acquisition (DAQ)

The Data AcQuisition (DAQ) consisted of three different systems. The RIBFDAQ system served as the master DAQ for the BigRIPS beam identificaiton DAQ, the TPC DAQ, the NeuLAND neutron wall DAQ, and the Kyoto Array DAQ systems. The TPC DAQ was handled by the NARVAL

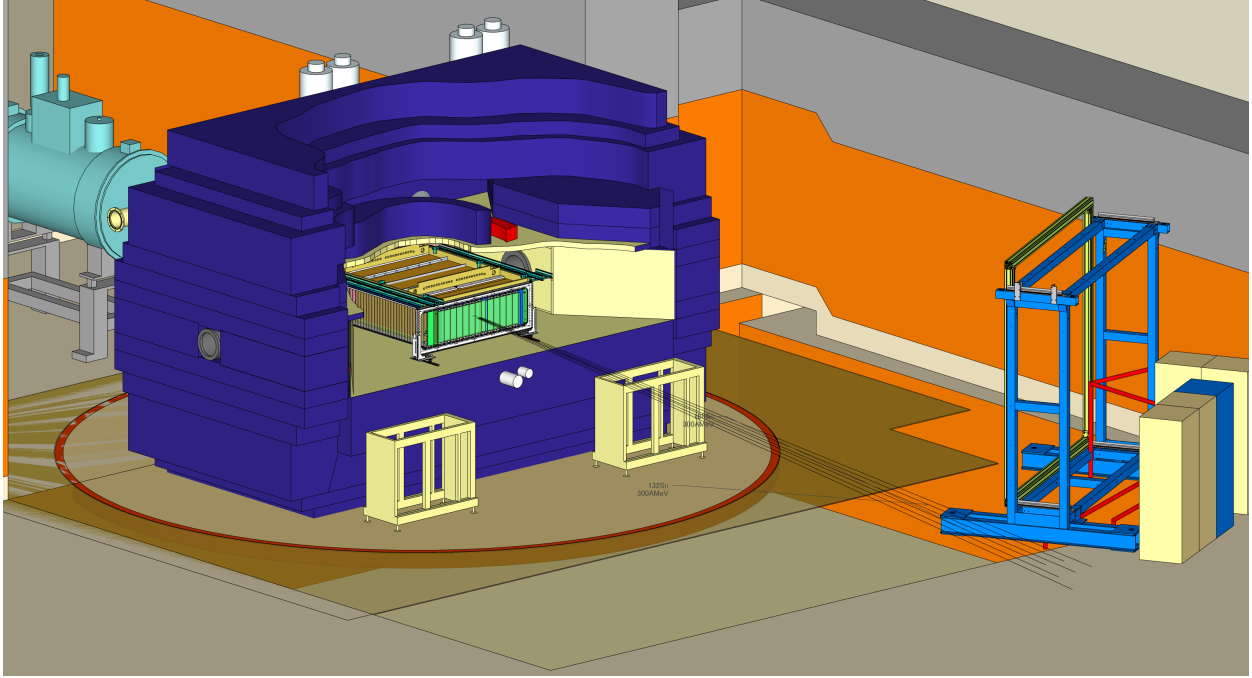


Figure 1.18: Drawing of the experimental setup with the TPC inside of the SAMURAI magnet at 0° configuration.

framework to readout the GET electronics for the S $\pi$ RIT TPC. A General Trigger Operator (GTO) trigger was supplied to each DAQ synchronizing the subsystems.

## 1.9 Trigger Condition

Signals from all of the auxiliary detectors were combined into several logic combinations to form a trigger logic for triggering the data acquisition (DAQ) to record data. An upstream scintillating bar formed the start counter signal, triggering on any beam coming down the beam line. The active veto will trigger for any beam that is incident off the target location. The KATANA veto produces a signal if the beam passed through the TPC un-reacted, causing no nuclear collision; this produces a veto signal with a width of 4  $\mu$ s which is the approximate time it takes for the beam to drift and clear the field cage volume. The Kyoto multiplicity trigger produces a signal when the total number of tracks passing through both Kyoto arrays are greater than 4.

There were several special trigger considerations when we built the trigger for the TPC. We

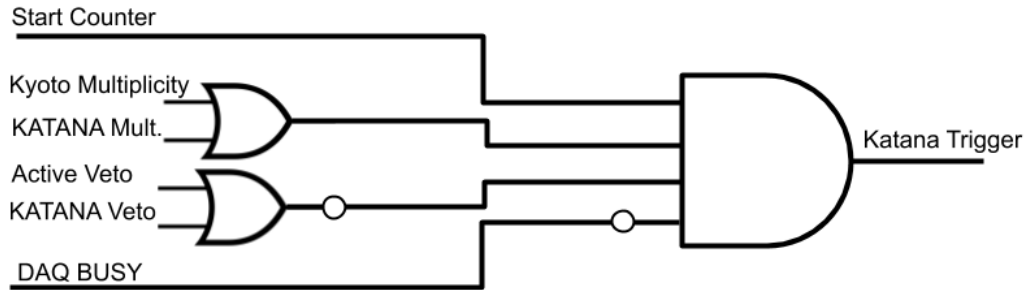


Figure 1.19: KATANA trigger box logic.

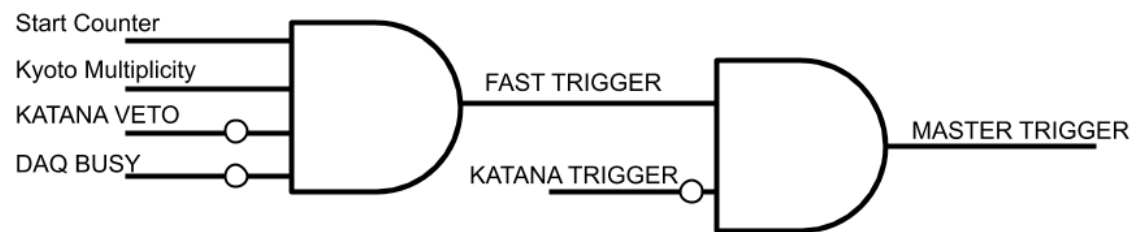
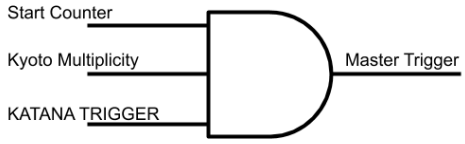
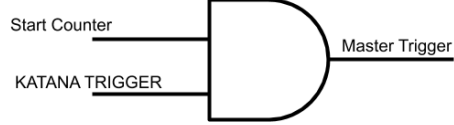


Figure 1.20: Master trigger logic.



(a)  $^{124}\text{Xe}$  primary beam trigger.



(b)  $^{238}\text{U}$  primary beam trigger.

required that the gating grid be opened fast to not miss any signal; as soon as there was a condition satisfying the Start Counter, Kyoto Multiplicity, the DAQ was not busy, and there was not a KATANA Veto signal. This was referred to as the Fast Trigger. If the KATANA trigger box is not satisfied –described later– this will trigger a Fast Clear signal which will not trigger the DAQ and will quickly close the gating grid. Figure 1.20 shows the logic of both of these triggers.

The master trigger for the DAQ was different for each primary beam as the experiment got progressively better. During the  $^{124}\text{Xe}$  primary beam, the KATANA trigger box was an input into the trigger logic where as in the  $^{238}\text{U}$  primary beam, the KATANA trigger box functioned as the trigger logic utilizing the internal trigger electronics. In either case the differences in the trigger were very minor and they both behaved practically the same except for minor details on the gating grid trigger [3]. Figure 1.19 summarizes the KATANA trigger box logic.

Figure 1.21a summarizes the  $^{132}\text{Xe}$  primary beam, where the condition to produce a true KATANA trigger output was there must be a Start Counter, KATANA multiplicity, no Veto, and no DAQ busy signal. The KATANA trigger, Kyoto Multiplicity, and Start Counter together trigger the DAQ.

Where as Fig. 1.21b summarizes the  $^{132}\text{Xe}$  primary beam, where the condition to produce a true KATANA trigger output was there must be a Start Counter, Kyoto or KATANA multiplicity, no Veto, and no DAQ busy signal. Here the KATANA trigger and the SC SUM??? together trigger the DAQ.

It is worth mentioning how the busy signals for the experiment were handled. The DAQ system

itself produces a busy signal which was combined with the busy signals from either opening or closing the gating grid. When opening the gating grid it is assumed the full volume of the TPC will be read out and therefore a 11  $\mu$ s gate is produced; which is slightly more than the time it takes for all the electrons to drift in the field cage. In the case where the gating grid should be fast closed, either due to the fast clear circuit or the end of the TPC measurement, a 5  $\mu$ s gate is produced to allow for the gating grid to settle to a closed configuration and clear the drift volume of any residual electrons from the beam. Both of these gates are included with the DAQ in an OR configuration which makes the overall busy signal.

## 1.10 Collision Data Taken

## **APPENDIX**

**APPENDIX**  
**RUNS ANALYZED IN THIS DATA**

System	#runs	Run numbers
$^{132}\text{Sn} + ^{124}\text{Sn}$	113	2841, 2843, 2844, 2845, 2846, 2848, 2849, 2850, 2851, 2852, 2855, 2856, 2857, 2858, 2859, 2860, 2861, 2875, 2877, 2878, 2879, 2880, 2881, 2882, 2883, 2884, 2887, 2888, 2889, 2890, 2891, 2892, 2893, 2894, 2896, 2898, 2899, 2900, 2901, 2902, 2903, 2904, 2905, 2907, 2914, 2916, 2917, 2919, 2920, 2921, 2922, 2924, 2925, 2926, 2927, 2929, 2930, 2931, 2932, 2933, 2934, 2935, 2936, 2939, 2940, 2941, 2942, 2943, 2944, 2945, 2946, 2948, 2955, 2956, 2958, 2959, 2960, 2961, 2962, 2964, 2965, 2966, 2968, 2969, 2970, 2971, 2972, 2973, 2975, 2976, 2977, 2978, 2979, 2980, 2981, 2982, 2983, 2984, 2985, 2986, 2988, 2989, 2990, 2991, 2992, 2993, 2997, 2999, 3000, 3002, 3003, 3007, 3039
$^{124}\text{Sn} + ^{112}\text{Sn}$	60	2542, 2543, 2544, 2546, 2547, 2548, 2552, 2553, 2554, 2555, 2556, 2557, 2558, 2559, 2560, 2562, 2563, 2564, 2565, 2566, 2567, 2568, 2569, 2570, 2571, 2572, 2573, 2574, 2575, 2578, 2579, 2580, 2581, 2582, 2583, 2584, 2585, 2586, 2587, 2588, 2589, 2590, 2591, 2592, 2593, 2594, 2595, 2596, 2597, 2598, 2599, 2600, 2601, 2617, 2618, 2619, 2620, 2621, 2622, 2623
$^{112}\text{Sn} + ^{124}\text{Sn}$	68	3059, 3061, 3062, 3065, 3066, 3068, 3069, 3071, 3074, 3075, 3076, 3077, 3078, 3080, 3081, 3082, 3083, 3084, 3085, 3087, 3088, 3089, 3090, 3091, 3092, 3093, 3094, 3095, 3097, 3098, 3102, 3103, 3138, 3139, 3140, 3141, 3142, 3143, 3144, 3145, 3146, 3148, 3149, 3150, 3151, 3152, 3153, 3154, 3155, 3156, 3157, 3158, 3159, 3165, 3166, 3167, 3168, 3169, 3170, 3171, 3172, 3177, 3179, 3180, 3181, 3182, 3183, 3184
$^{108}\text{Sn} + ^{112}\text{Sn}$	85	2272, 2273, 2274, 2275, 2276, 2283, 2284, 2285, 2286, 2288, 2289, 2291, 2310, 2311, 2314, 2315, 2320, 2322, 2323, 2324, 2325, 2331, 2332, 2333, 2334, 2335, 2336, 2337, 2340, 2341, 2362, 2363, 2368, 2369, 2370, 2371, 2372, 2373, 2374, 2375, 2378, 2379, 2380, 2381, 2382, 2383, 2384, 2385, 2386, 2387, 2388, 2389, 2391, 2392, 2393, 2394, 2395, 2396, 2397, 2398, 2399, 2400, 2401, 2402, 2429, 2432, 2433, 2434, 2437, 2438, 2439, 2440, 2442, 2453, 2461, 2462, 2463, 2501, 2502, 2503, 2505, 2506, 2507, 2508, 2509

Table .1: List of runs for the analysis.

## **APPENDIX**

### **SECOND APPENDIX**

## **BIBLIOGRAPHY**

## BIBLIOGRAPHY

- [1] Y. Yano, The ri beam factory project: A status report, Nucl. Instrum. Meth. B 261 (1-2) (2007) 1009–1013. doi:10.1016/j.nimb.2007.04.174.
- [2] T. Kobayashi, et al., Samurai spectrometer for ri beam experiments, Nucl. Instrum. Meth. B 317 (2013) 294–304. doi:10.1016/j.nimb.2013.05.089.
- [3] J. E. Barney, Charged pion emission from  $0rw1s34rfesdcfkexd09rt31121rw1s34rfesdcfkexd09rt3sn$  +  $0rw1s34rfesdcfkexd09rt31241rw1s34rfesdcfkexd09rt3sn$  and  $0rw1s34rfesdcfkexd09rt31241rw1s34rfesdcfkexd09rt3sn$  +  $0rw1s34rfesdcfkexd09rt31121rw1s34rfesdcfkexd09rt3sn$  reactions with the srit time projection chamber, Ph.D. thesis, copyright - Database copyright ProQuest LLC; ProQuest does not claim copyright in the individual underlying works; Last updated - 2019-11-05 (2019). URL <http://ezproxy.msu.edu.proxy1.cl.msu.edu/login?url=https://search-proquest-com>.
- [4] W. Blum, W. Riegler, L. Rolandi, Particle Detection with Drift Chambers, Springer, Berlin, Heidelberg, 2008.
- [5] E. Pollacco, et al., Get: A generic and comprehensive electronics system for nuclear physics experiments, Physics Procedia 37 (2012) 1799–1804. doi:10.1016/j.phpro.2012.02.506.
- [6] L. Landau, On the energy loss of fast particles by ionization, J. Phys. USSR 8 (201).
- [7] P. Shulek, Fluctuations of ionization loss, Sov. J. Nucl. Phys 4.
- [8] H. Bichsel, Straggling of heavy charged particles: Comparison of born hydrogenic-wave-function approximation with free-electron approximation, Phys. Rev. B 1 (1970) 2854.
- [9] E. Gatti, et al., Optimum geometry for strip cathodes or grids in mwpc for avalanche localization along the anode wires, Nucl. Instr. Meth. Phys. Res. A 163 (1979) 83–92. doi:10.1016/0029-554X(79)90035-1.